Materials Science & Engineering A 908 (2024) 146771

Contents lists available at ScienceDirect

Materials Science & Engineering A

journal homepage: www.elsevier.com/locate/msea

Exploring high-temperature deformation and damage behaviour in high-performance ferritic (HiperFer^{SCR}) steel with Laves phase particles

Atef Hamada [a,b], Fadoua Aarab [a], Ruth Schwaiger [a], Tarek Allam [a,*,1]

[a] Institute of Energy and Climate Research: Structure and Function of Materials (IEK-2), Forschungszentrum Jülich GmbH, 52425, Jülich, Germany
[b] Kerttu Saalasti Institute, Future Manufacturing Technologies, University of Oulu, Pajatie 5, FI-85500, Nivala, Finland

ARTICLE INFO

Keywords:
HiperFer steel
Laves phase
High-temperature deformation
Damage behaviour
Microstructure
Slip bands

ABSTRACT

The mechanical behaviour at high temperatures and the corresponding microstructural characteristics of a newly developed high-performance ferritic, salt-corrosion-resistant (HiperFer^{SCR}) steel containing Laves phase particles were studied to investigate the active deformation mechanisms and the evolution of damage. A series of tensile tests were conducted at both room temperature and elevated temperatures (550, 600, and 650 °C), along with detailed microstructural analyses using scanning electron microscopy and electron backscatter diffraction. The tensile flow characteristics of HiperFer^{SCR} at room temperature exhibit significant strain hardening, which is due to the Laves phase particles that encourage planar slip, demonstrated by the formation of numerous slip bands and low-angle grain boundaries. The intersections of these slip bands with grain boundaries appear to be the initiation sites for cracks, which then propagate intergranularly as well as within grain interiors along the slip bands. At high temperatures, the flow characteristics show strain softening, which is attributed to a dynamic recovery (DRV) mechanism, evident in the formation of subgrain boundaries decorated with Laves phase particles. During high-temperature deformation, damage initiates in the particle-free zone (PFZ), which expands at higher temperatures, leading to strain localisation, void formation along the grains, and eventually, grain boundary decohesion.

1. Introduction

Steel alloys have played a pivotal role in modern engineering and industry due to their exceptional strength, versatility, and adaptability. They are indispensable in a wide range of applications, from towering skyscrapers and complex machinery to high-speed transportation systems and cutting-edge industrial processes. However, traditional ferritic stainless steels with high chromium content, while praised for their excellent resistance to high-temperature oxidation [1–4], are often considered non-hardenable, limiting their suitability for structural applications at elevated temperatures. To address this limitation, a high-chromium ferritic steel called HiperFer (High-Performance Ferrite) has been developed. With a chromium content of 17 wt% to 19 wt%, HiperFer surpasses conventional ferritic-martensitic steels, which contain 9–12 wt% chromium, in several key aspects, including creep strength, thermomechanical fatigue resistance, and steam oxidation resistance [5–8]. HiperFer's development was inspired by the success of Crofer® 22H, a commercially viable steel originally designed for use in interconnector plates within Solid Oxide Fuel Cells (SOFC) [9,10].

The HiperFer alloy is renowned for its reinforcement through the precipitation of finely dispersed intermetallic Laves phase particles, specifically (Fe, Cr, Si)2(Nb, W) [11,12]. Laves phases form a significant class of intermetallic compounds that are typically considered undesirable and, therefore, to be avoided in high-temperature steels [13]. However, with precise control over the precipitation process, the Laves phase can act as a strengthening agent [14–16]. Additionally, when precipitated along grain boundaries, the Laves phase can effectively inhibit grain growth at higher temperatures, leading to long-term enhancement of high-temperature strength [17]. In HiperFer steels, Laves phase particles typically act as barriers to the dislocation motion, impeding their movement and thereby enhancing strength at ambient temperatures through particle strengthening mechanism [10]. Studies on super ferritic stainless steels have demonstrated that controlling Laves phase precipitations during annealing heat treatment can achieve a favourable balance of strength and ductility [18]. Laves phase particles can contribute to the strengthening by impeding the grain boundary

---

* Corresponding author.
E-mail address: t.allam@fz-juelich.de (T. Allam).
[1] On an unpaid leave from Department of Metallurgical and Materials Engineering, Suez University, 43,528, Suez, Egypt.

https://doi.org/10.1016/j.msea.2024.146771
Received 13 February 2024; Received in revised form 5 May 2024; Accepted 2 June 2024

sliding, thereby enhancing creep resistance and inhibiting recrystallization [11]. Similarly, investigations into FeCrAl alloys have revealed that deformation microstructures, as well as recrystallised and recovered microstructures, are influenced by the pinning effect of Laves phases relative to annealing temperatures [19]. In high-Cr fully ferritic steels, the formation of PFZ along high-angle grain boundaries has been observed [5]. Within these PFZs, material deformation behaviour differs from that of the grain interiors, which are strengthened by Laves phase particles. Variations in chemistry and dislocation densities within PFZs are believed to contribute to creep void formation and the premature failure at high temperatures [7]. The key elements forming the Laves phase—W, Nb, and Si—have a significant impact on mechanical properties. Nb plays a crucial role in the precipitation of the Laves phase [5, 11,13] and helps prevent the formation of chromium carbides at grain boundaries, which could otherwise lead to intergranular corrosion [20]. W contributes to solid solution strengthening and increases the volume fraction of the Laves phase [5]. Si not only promotes the formation of the Laves phase and stabilises it [21], but also extends the lifespan of Fe–Cr steel components by enhancing the adhesion of protective oxide layers [22].

A notable evolution of HiperFer is the HiperFer^{SCR} (Salt Corrosion Resistant) variant, strategically engineered for application in solar salt melts within Concentrated Solar Power (CSP) plants and thermal energy storage (TES) systems [23]. The addition of Al in HiperFer^{SCR} results in a self-passivating effect, forming a compact Al_2O_3 protective layer that offers significantly higher corrosion resistance to solar salt compared to Cr_2O_3. The corrosion behaviour of HiperFer^{SCR} has been addressed in other studies [24]; therefore, it is not the focus of this study. Additionally, it has also been noted that aluminium, as a Laves phase former, generally adds complexity to the alloy's behaviour [25], but its role in HiperFer^{SCR} steel is still under investigation.

As the mechanical properties of HiperFer steel, such as strength, creep resistance, and thermal fatigue resistance, have been addressed in previous studies [11], the current study focuses on exploring the deformation and damage mechanisms inherent in the new HiperFer variant, HiperFer^{SCR}. In this study, tensile tests were conducted at room temperature and within the expected operating temperature range of 550–650 °C. The deformed microstructures at both room and high temperatures were analysed to establish the correlations between the observed microstructural features and the active hardening or softening mechanisms, considering the role of Laves phase particles. The variations in damage evolution during deformation at different temperatures were investigated, and these differences will be discussed based on the fracture surface characteristics and deformation-induced features.

2. Experimental procedures

2.1. Materials

The HiperFerSCR 17Cr18 alloy examined in this study was produced in the controlled environment of the Vacuum Furnace VI-3 at the Steel Institute of RWTH Aachen University. The molten steel was cast into ingots measuring 550 × 140 × 140 mm^3. The ingots were then homogenised at 1250 °C for 2 h. The chemical composition of the produced ingot, as shown in Table I, was determined using inductively coupled plasma–optical emission spectroscopy (ICP-OES). The steel ingots underwent hot forging, followed by hot rolling to a final thickness of 15 mm. The hot-rolled material was subjected to solution treatment at 1100 °C for 15 min. To adjust the microstructure, a double aging treatment (DAT) was applied to the HiperFer^{SCR} steel. During the DAT process, the microstructure of HiperFer^{SCR} undergoes significant changes, notably the formation of Laves phase precipitates, which feature a nanoscale-shaped morphology that contributes to the overall strengthening mechanism of the steel under consideration. The first aging step involved heating to 540 °C for 5 h, followed by water quenching. This step is applied to reduce the area of PFZ at the grain boundaries. The second aging step involved heating to 650 °C for 10 h, again followed by water quenching. The relatively high-temperature aging at 650 °C in the second stage is the design temperature of the HiperFer steels, which was chosen as the principal precipitation heat treatment step to achieve the optimum Laves phase precipitation. The specific thermomechanical cycle sequences, as depicted in Fig. 1, were selected to achieve distinct objectives.

The steel ingots first underwent homogenisation (HG) at 1250 °C to reduce micro-segregation of alloying elements, ensuring uniformity in composition throughout the material. Next, hot forging (HF) was used to break down the dendritic cast structure, promoting a finer grain structure, which is essential for enhancing mechanical properties. After hot forging, hot rolling was employed to refine the grain structure further and achieve a final thickness of 15 mm for subsequent testing. This step helps improve the material's mechanical properties and dimensional stability.

The hot-rolled material was then subjected to a solution treatment at 1100 °C to dissolve any unwanted second-phase particles that may have precipitated during previous processing stages. This treatment is designed to optimise the microstructure for improved performance. Finally, DAT was applied to promote the formation of intermetallic Laves phase particles. These particles are key to enhancing the high-temperature strength and resistance to creep deformation in the steel under study.

2.2. High-temperature tensile tests

To evaluate the high-temperature mechanical properties of the newly developed steel, tensile tests were conducted at 550 °C, 600 °C, and 650 °C, and compared with the mechanical properties at room temperature. Round tensile specimens with a gauge length of 20 mm and a diameter of 3 mm were machined from the processed steel plates in the rolling direction. The geometry of these tensile specimens is shown in Fig. 2. The non-standard geometry and dimensions of the hot tensile specimens were chosen to suit the setup of the tensile machine, particularly for testing at high temperatures. The main focus of our study is to characterise the deformation and fracture mechanisms of the developed steel under high-temperature conditions relevant to its intended applications. While the test specimens' specific geometry might differ from standard practices, this choice does not affect the mechanisms being investigated. The tensile tests were carried out by controlling the crosshead displacement at a constant rate of $5.5 \times 10^{-6}\ s^{-1}$ using an Instron (Norwood, MA, USA) 1362 testing machine with a 10 kN load cell.

2.3. Microstructural analysis

To examine the active deformation mechanisms and damage behaviours of HiperFer^{SCR} steel during high-temperature tensile tests, Electron Backscatter Diffraction (EBSD, HKL NordlysNano, Oxford Instruments, High Wycombe, UK) was used on tested specimens at various temperatures, operating within a field-emission scanning electron microscope (FE-SEM, Zeiss Supra 50VP). EBSD was conducted at an accelerating voltage of 15 kV, with a working distance of 12 mm, and

Table 1
Chemical composition determined by inductively coupled plasma–optical emission spectroscopy (ICP-OES) of the investigated HiperFer^{SCR} steel, in wt. %.

Alloy	Cr	W	Nb	Mn	Si	Al	C	Fe
HiperFer^{SCR}	17.20	2.87	0.63	0.51	0.42	3.44	<0.01	Bal.

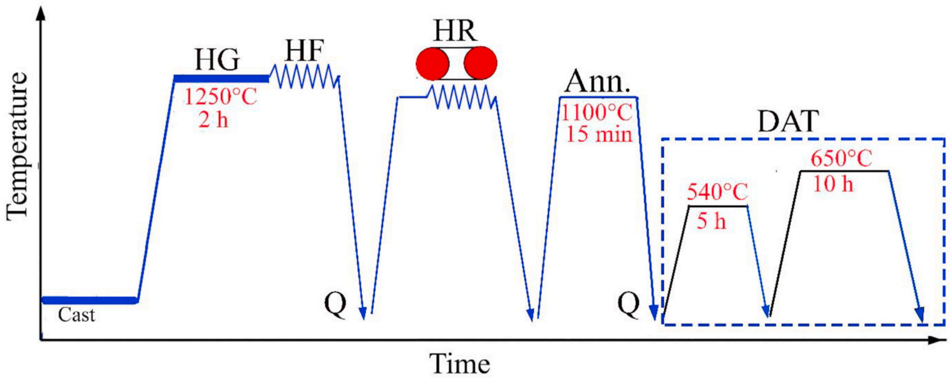

Fig. 1. Schematic representation of the process route applied to adjust the final microstructure of the investigated HiperFer^{SCR} steel. (HG: homogenisation, HF: hot forging, HR: hot rolling, Ann.: annealing, Q: water quench, DAT: double aging treatment).

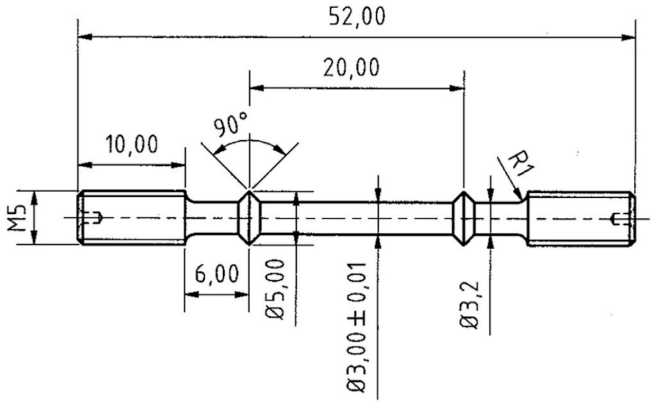

Fig. 2. Schematic of tensile specimen for high-temperature slow strain rate tests with dimensions given in millimeters.

fine step sizes of 0.1 μm and 0.5 μm for high- and low-magnification mapping, respectively. Energy-Dispersive X-ray Spectroscopy (EDS) was used to determine the average chemical composition of the formed Laves phase. For microstructure analysis, the tested tensile specimens were sectioned parallel to the direction of straining, followed by standard metallographic preparation methods, including mechanical grinding and polishing down to a 1 μm finish with diamond suspension. The specimens were then chemically polished using a colloidal suspension of silica with a particle size of 0.05 μm.

Various deformation features, such as slip bands, deformation bands, substructures, and crack initiation sites, were observed near the fracture surfaces of specimens tested at both room and high temperatures. To maintain the consistency in the selection of areas for deformation analysis, the investigations were carried out on specimens from the corresponding gauge lengths at a constant distance of 2 mm from the edge of fracture. Additionally, the fracture surfaces were analysed to identify the predominant fracture mode and to understand the correlations between the deformation and damage mechanisms.

3. Results and discussion

3.1. Initial microstructure

The initial microstructure of HiperFer^{SCR} steel is a crucial starting point for understanding its mechanical behaviour. To gain an insight into these finer details, we employed a combination of EBSD mapping and backscattered electron (BSE) imaging. The microstructure resulting from the thermomechanical process is illustrated in Fig. 3. It is fully ferritic, featuring relatively large grains, as illustrated in Fig. 3(a). A notable characteristic of this microstructure is the presence of abnormally large grains, with sizes reaching 0.5 mm. This occurrence can be attributed to the high-temperature homogenisation treatments at 1250 and 1125 °C, which were carried out to dissolve large precipitates induced by previous forging and hot-rolling processes. At such elevated temperatures, recovery and grain coarsening in body-centred cubic (bcc) ferrite occur at an accelerated rate, resulting in predominantly coarse grains [26,27]. Moreover, the alloy design of HiperFer steels [28] only allows for a ferritic phase throughout the processing and application temperature range, avoiding phase transformations that could refine the grain structure. This avoidance of phase transformation is actually beneficial for welding, as it prevents type IV cracking caused by re-transformation and grain refinement in the heat-affected zone [29].

The grain-size distribution of the resulting microstructure after thermomechanical processing is shown in Fig. 3(b). The structure mainly comprises coarse grains, spanning a range from 0.5 mm to 0.9 mm, constituting roughly 25 % of the grain structure. The remaining 75 % of the grains fall within the 0.4–0.1 mm size range. As a result, the average grain size of the investigated HiperFer^{SCR} stands at approximately 300 μm [30].

A more detailed view of the microstructure can be seen in the orientation map presented as an inverse pole figure (IPF) in Fig. 3(c). This map indicates a slightly textured microstructure resulting from the high-temperature thermomechanical treatment. The orientation map is explained by the colour key in the lower-right corner of Fig. 3(c). The coarse-grain structure predominantly exhibits a random texture, with crystallographic orientations aligned with<101> (green) and <001> (red). Variations in the orientations of adjacent grains may be due to the high-temperature treatment applied during the thermomechanical processing of the steel. This treatment seems to limit the influence of deformation on the texture, as evidenced by the low proportion of low-angle grain boundaries (LAGBs) in the microstructure, as shown in Fig. 3 (c). It's well known that grain boundary type can affect the crystallographic orientation of the grains [31].

To closely examine the microstructure through high-magnification backscattered electron (BSE) imaging, Fig. 3(d) reveals a key characteristic of the adjusted microstructure for HiperFer^{SCR} steel: the nanoscale precipitation of the Laves phase, dispersed throughout the matrix with a high number density. These precipitates have a spheroidal shape with an average equivalent diameter of about 80 ± 30 nm. The collective presence of these precipitates plays a significant role in boosting the overall strength of the steel and greatly influences its mechanical properties. Unlike advanced ferritic-martensitic steels containing 9–12 wt% Cr that are strengthened by MX carbonitride particles [30], HiperFer steels with a fully ferritic matrix and limited solubility of carbon and nitrogen are typically strengthened by Laves phases. This finding aligns with previously documented results within the existing body of literature [32,33]. A notable feature of the grain structure is the

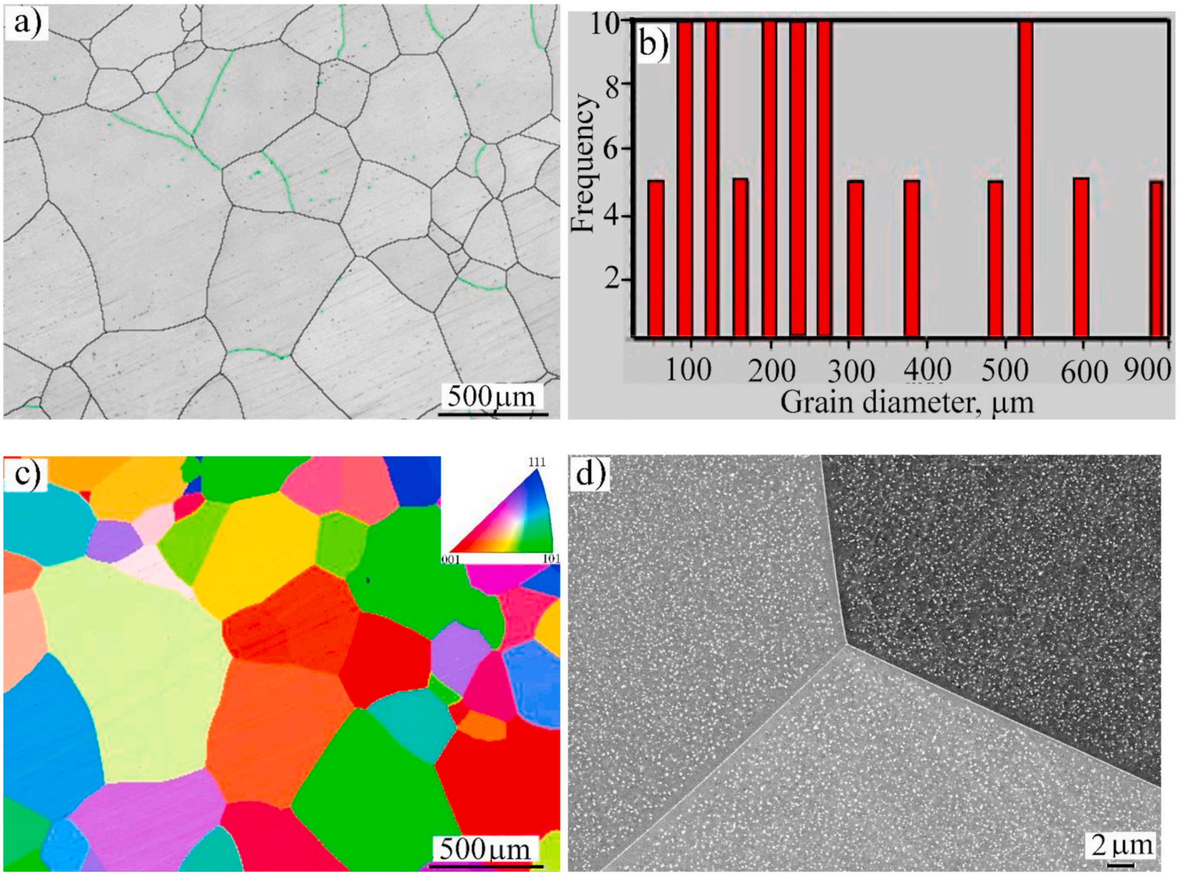

Fig. 3(a). Initial microstructure of HiperFer^{SCR} steel following thermomechanical processing: (a) EBSD-image quality map superimposed with misorientation map and LAGBs in green, (b) Grain size distribution of the observed microstructure, (c) EBSD-orientation map of (a), and (d) BSE micrograph of the nanoscale Laves phase precipitates. (For interpretation of the references to colour in this figure legend, the reader is referred to the Web version of this article.)

absence or scarcity of Laves phase particles in the areas adjacent to the grain boundaries. These regions, commonly known as the PFZ, have an average width of about 340 ± 80 nm, as depicted in Fig. 4(a). The mechanism behind the formation of the PFZ around grain boundaries is a crucial aspect of the microstructure. In our study, we observed that grain boundaries are largely devoid of precipitates, while Laves phase particles are primarily found within the grain interiors. This observation implies that during the initial hot processing stages of the steel, such as hot forging and hot rolling, dynamic recovery processes are activated due to the high stacking fault energy of the ferritic matrix. As a result of these processes, LAGBs are formed within the grain interiors, providing favourable sites for the precipitation of Laves phase particles. This leads to the formation of PFZs surrounding the high-angle grain boundaries (main boundaries), which significantly contributes to the overall microstructural characteristics of the steel. The size distribution of the Laves phase particles is shown in Fig. 4(b).

The EDS analysis was conducted to examine the chemical composition of Laves phase particles in HiperFer^{SCR} steel. To ensure accuracy, EDS analysis was conducted on large Laves phase particles resulting from a distinct heat treatment, as shown in Fig. 5(a), using a low accelerating voltage of around 5 kV. The EDS spectra for the matrix and Laves phase particles are shown in Fig. 5(b) and (c), respectively. The results, detailed in Table II, highlight significant concentrations of two key elements: Nb and W. Nb accounts for approximately 28 wt%, while

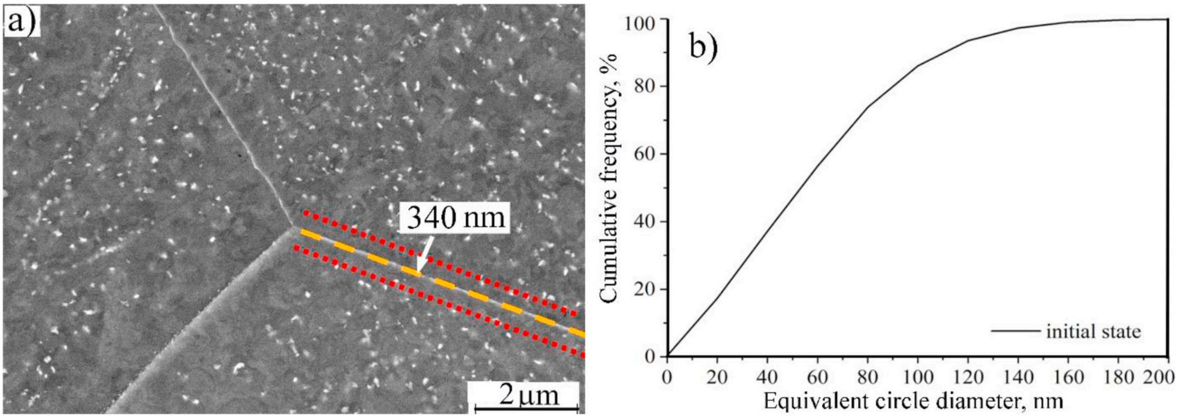

Fig. 4. (a) High magnification of initial microstructure shows the typical size of PFZ, and (b) size distribution of Laves phase particles.

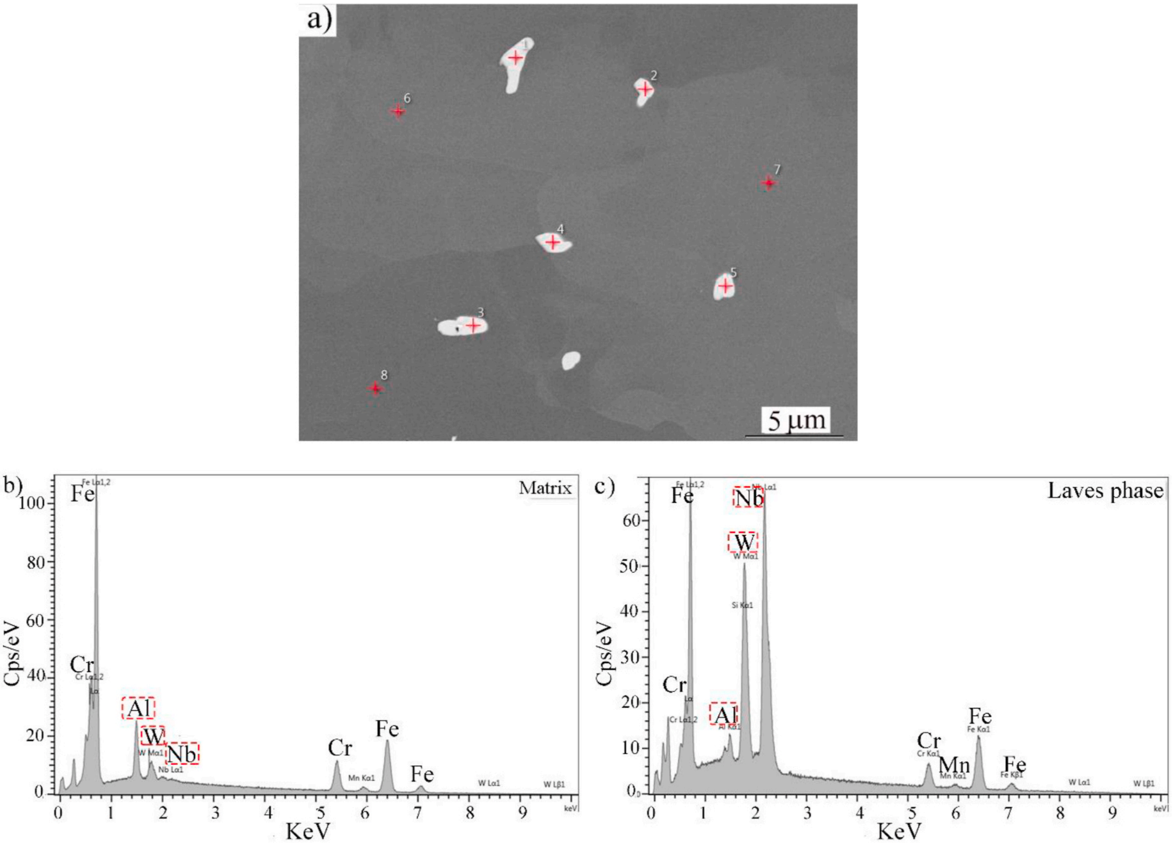

Fig. 5. EDS analysis of the microstructure constituents in HiperFer^{SCR} steel: (a) BSE image of the examined region, (b) EDS spectrum of the matrix, and (c) EDS spectrum of the Laves phase particle.

Table 2
Average chemical composition of Laves phase in HiperFer^{SCR} steel (wt.%) determined by EDS, highlighting significantly high Nb and W concentrations compared to the matrix.

Element	Al	Si	Cr	Mn	Fe	Nb	W
Laves phase	0.71 ± 0.04	1.86 ± 0.14	8.3 ± 0.26	0.31 ± 0.19	44.65 ± 0.87	28.04 ± 0.88	16.15 ± 1
Ferritic matrix	3.14	0.23	17.13	0.73	75.8	0.4	2.6

W contributes around 16 wt%. These elements play pivotal roles in forming Laves precipitates. Nb is a strong Laves phase former [34] with low solubility [35] and high diffusivity [36] in ferrite, making it a key component in Laves phase formation. Furthermore, co-alloying with W and Si results in a thermodynamically stable Laves phase of type (Fe, Cr, Si)$_2$(Nb, W) [37,38]. In addition to Nb and W, the Laves phase in HiperFer^{SCR} steel includes a moderate Cr content of approximately 8 wt % with lower Si and Al contents of about 2 and 0.7 wt%, respectively. Although Si and Al are not as predominant as Nb and W, they contribute to the solid solution strengthening of the matrix. Si has been found to promote the nucleation of Nb-containing Laves phase [39], but the role of Al in Laves phase precipitation is still unclear and requires further investigation, which will be explored in future studies.

As HiperFer steels are designed to maintain a fully ferritic microstructure over the entire temperature range, they are expected to exhibit relatively poor mechanical properties in the as-processed state, which can limit their applications. Therefore, precipitation annealing heat treatments are applied to tailor the microstructures and allow the formation of fine Laves phase particles (both intra-granular and inter-granular), which effectively enhance the overall mechanical properties. Engineering the formation of these Laves phase particles and the PFZ along high-angle grain boundaries (HAGBs) is crucial for optimising the creep resistance [7]. In this study, the formation of the Laves phase is closely linked to the high-temperature DAT it undergoes during the thermomechanical cycle, as depicted in Fig. 1. DAT temperatures provide the energy required for atomic diffusion and phase transformation, which are essential for enhancing the precipitation of the Laves phase in the HiperFer^{SCR} matrix. It was demonstrated that an annealing heat treatment in the temperature range between 600 and 650 °C for 0.5 up to 10 h can be utilised for precipitation of Laves phase particle in HiperFer steels [11]. The stability of Laves phase particles at high temperatures, such as 650 °C, is an important consideration. Laves phase formation is primarily correlated with the presence of alloying elements such as W and Nb. As a result, the formed Laves phase particles exhibit high stability at elevated temperatures, including 650 °C. However, over prolonged exposure times, some particles may experience growth and subsequently lose their cohesivity with the matrix, which could affect the overall microstructural stability of the steel.

3.2. High-temperatures tensile properties

Fig. 6 presents the engineering stress–strain curves illustrating the tensile behaviour of the HiperFer^{SCR} steel under various test temperatures. Notably, the flow stresses decrease with an increase in the test temperature, which conforms to the classic deformation characteristics exhibited by steels at elevated temperatures. In the high temperature range of 550–650 °C, as the temperature increases, the flow curves display a diminishing trend. However, at room temperature, the flow curve exhibits a significant hardening during the plastic deformation stage, which persisted up to the point of ultimate stress. At higher temperatures, clear peaks in the flow-stress curves emerge at

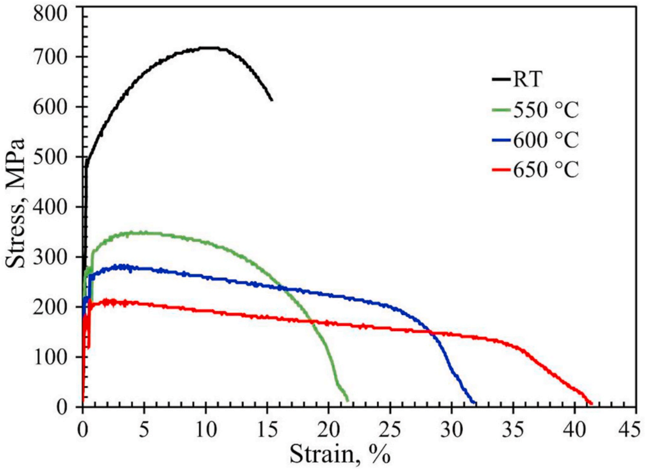

Fig. 6. Engineering stress–strain curves for HiperFer^{SCR} steel at various test temperatures, namely, room temperature (RT), 550 °C, 600 °C, and 650 °C.

deformation strains of approximately 2 %. Subsequently, the flow stress gradually declined. These distinct patterns indicate the occurrence of high-temperature dynamic softening. Table III lists the variations in the tensile properties with the applied test temperatures. At room temperature, the HiperFer^{SCR} steel exhibits a high yield strength (Rp 0.2) of 494 MPa and a tensile strength (Rm) of 717 Mpa, while it exhibits a relatively low ductility, which might impair its impact toughness. The enhanced strength of the steel at RT is attributed to a combination of solid-solution strengthening and precipitation strengthening facilitated by the formation of Laves phase particles. Mechanical strength gradually decreases with increasing test temperature, reaching 175 MPa for yield strength and 213 MPa for tensile strength at 650 °C. It is known that the hot deformation of α-bcc ferrite is notably facile, resulting in a softer response. This characteristic is attributed to the high stacking fault energy (SFE) of ferrite, which promotes dislocation recovery and the rapid annihilation and rearrangement of dislocations [40,41]. Further discussion on the softening mechanism in HiperFer^{SCR} based on microstructural analyses is provided in Section 3.3.

3.3. Deformed microstructures and deformation mechanisms

3.3.1. Microstructural characteristics after tensile testing at high-temperatures

The microstructure of the tested specimens was characterised using EBSD and BSE imaging to investigate the softening mechanism operating at high temperatures during tensile testing and the associated damage behaviour of HiperFer^{SCR} steel. As illustrated in Fig. 7, the microstructure shows the condition of the specimens after high-temperature tensile straining at 650 °C.

The image quality map presented in Fig. 7(a) shows relatively elongated ferritic grains aligned with the direction of tensile loading. The presence of LAGBs, depicted in green, is noticeable around the primary grain boundaries, highlighting the localisation of deformation strains in the PFZ. The IPF map in Fig. 7(b) reveals two key characteristics. First, the orientation map shows that most of the deformed grains predominantly retain <101> and <001> orientations, similar to those found in the undeformed microstructure. Second, several grains exhibit multiple colour zones, marked by white circles, suggesting the formation of subgrain structures during high-temperature deformation. The creation of subgrain structures in the alpha body-centred cubic (α-bcc) structure is associated with the recovery and rearrangement of dislocations [42–44] a process that significantly affects the microstructure after high-temperature deformation. Due to resolution limitations, the Laves phase particles could not be indexed by EBSD.

Table 3
Variation of the tensile properties of HiperFer^{SCR} steel with the temperature.

Tensile test temperature	RT	550 °C	600 °C	650 °C
Rp0.2	494	271	211	175
Rm	717	350	283	213

The failure to index nanosized Laves phase particles using EBSD can be attributed to two key factors. First, the spatial resolution of EBSD is typically insufficient to accurately capture diffraction patterns from nanosized particles. Second, there is interference between background signals from the surrounding matrix and the diffraction patterns produced by the nanosized precipitates.

To delve deeper into the connection between the Laves phase and deformed microstructure, we employed BSE imaging. Fig. 7(c) provides a revealing view of the microstructural changes induced during high-temperature tensile deformation. In this image, we note the emergence of a distinctive subgrain structure, which is notably augmented by the dynamic recovery (DRV) mechanism that becomes active during high-temperature tensile deformation. This mechanism involves the rearrangement of dislocations within the material, which leads to the formation of subgrains.

The appearance of subgrain boundaries decorated with Lave-phase particles are particularly intriguing. These arrangements of the Laves phase particles on the deformation-induced subgrain boundaries are indicated by the yellow circles in Fig. 7(c). The Laves phase particles tended to cluster along these subgrain boundaries, creating a pinning effect. This implies that the Laves phase particles effectively anchor themselves at these boundaries, which, in turn, hinders the occurrence of dynamic recrystallization (DRX). DRX typically results in the formation of new finer recrystallised grains within the microstructure. However, because of the presence of Laves phase particles and their pinning effect at the substructural boundaries, we did not observe grain refinement in the microstructure. In essence, the Laves phase plays a crucial role in maintaining the existing grain structure and inhibiting the development of new fine recrystallised grains in this specific context.

Fig. 7(d) shows a longitudinal cross section of the fracture zone, providing significant insights into the fracture characteristics. Particularly noteworthy is a prominent feature: an elongated crack of considerable size that follows the boundaries of the ferrite grains, aligned at an approximate 45-degree angle relative to the loading axis (indicated by red arrows). Furthermore, a secondary observation in the image was the presence of a smaller crack initiated from the grain boundary. The damage behaviour is described and discussed in section 3.4 in details.

For the specimen tested at a relatively lower temperature of 550 °C, distinct microstructural characteristics became evident, as shown in Fig. 8. Within the deformed ferritic grains, a notable prevalence of LAGBs (<15 °C, depicted in green) is observed, as shown in Fig. 8(a). Simultaneously, slip bands featuring HAGBs, indicated by the black lines) were promoted within the grains, as indicated by the white circles. Grains lacking slip bands underwent the generation of subgrain boundaries. Two distinct cracks, Crack I and Crack II, are also observed. Crack I was initiated at a grain boundary site, marked by a red arrow, which coincided with the intersection with a slip band. Crack I propagated perpendicularly to the loading direction (indicated by red arrows). In contrast, crack II was initiated at the intersection site of the subgrain boundary with a slip band and propagated along the subgrain boundary.

Additionally, a Kernel Average Misorientation (KAM) map of the corresponding microstructure was presented to illustrate the degree of misorientation induced by the localised strain deformation within various zones of the microstructure [45,46]. The KAM map in Fig. 8 (b) highlights grains with slip bands that correspond to regions characterised by highly localised misorientation, resulting in elevated KAM values (depicted in green and yellow areas). This phenomenon is associated with high dislocation density, which is attributed to a significant degree of strain. This strongly suggests the occurrence of DRV which agrees with the observed enhancement of LAGBs within these grains, as

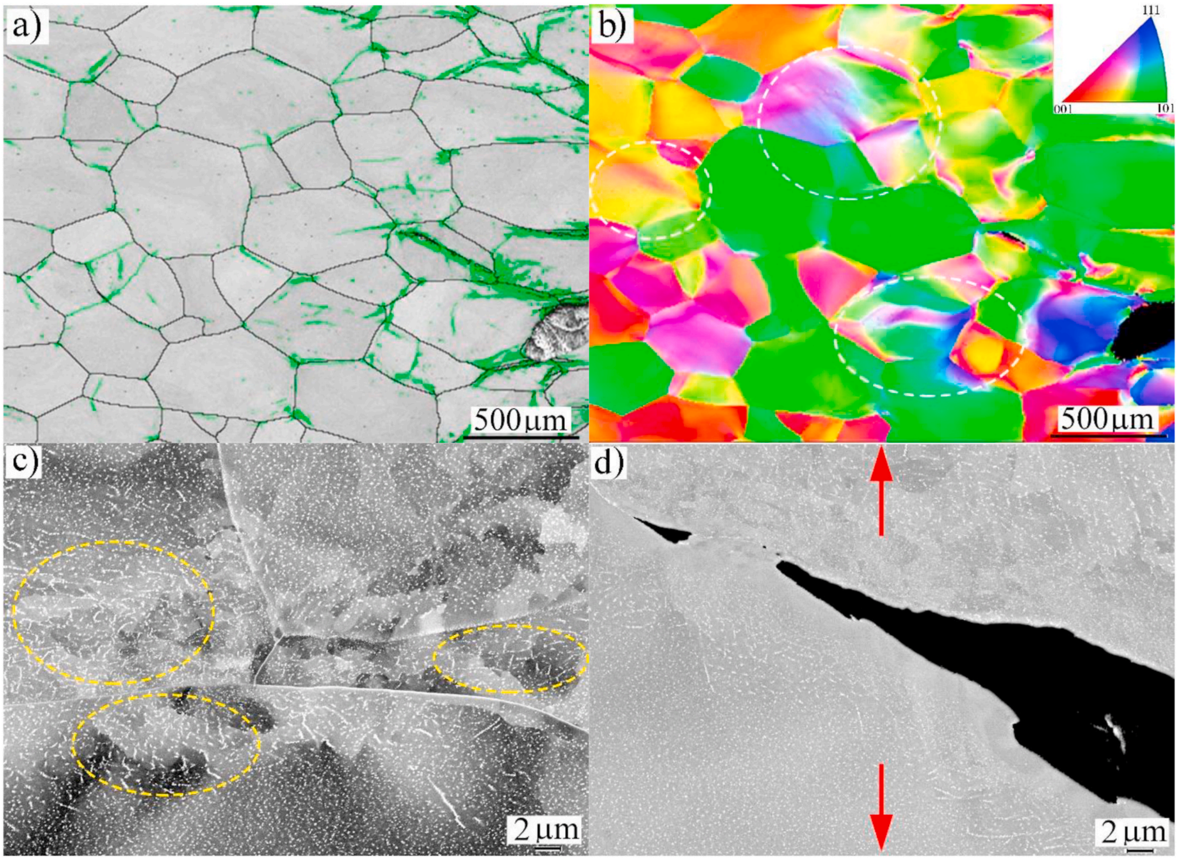

Fig. 7. Microstructural characteristics of HiperFer^{SCR} after tensile deformation at 650 °C: (a) EBSD-image quality map superimposed with the misorientation map (LAGBs in green), (b) EBSD-orientation map corresponding to (a), (c) High-magnification SEM-BSE image of the deformed zone showing the developed substructures decorated with Laves phase particles (indicated in yellow circles), and (d) longitudinal cross-section of the fracture zone revealing crack propagation along a grain boundary of a wide PFZ (red arrows indicate the loading direction). (For interpretation of the references to colour in this figure legend, the reader is referred to the Web version of this article.)

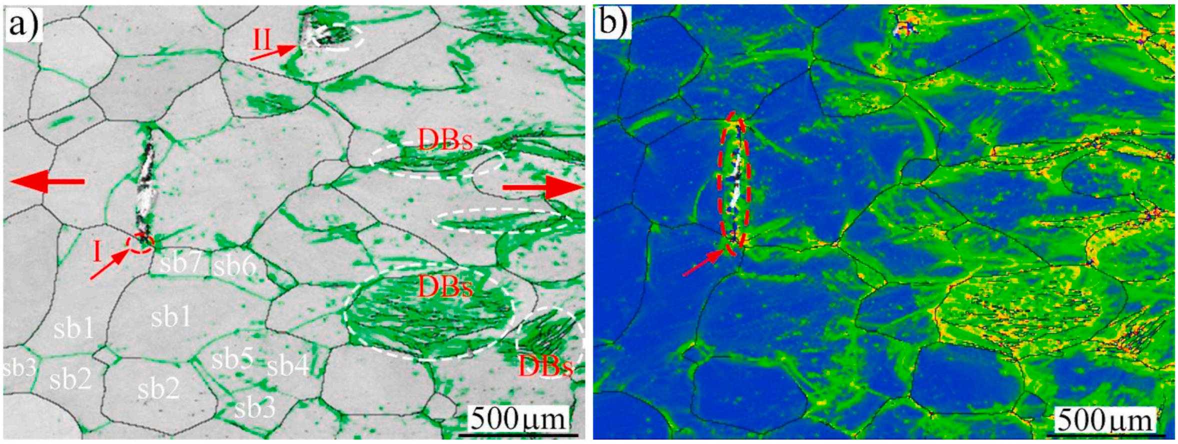

Fig. 8. Microstructural characteristics of HiperFer^{SCR} after tensile deformation at 550 °C: (a) EBSD-IQ Map superimposed with the misorientation map (red arrows indicate the loading direction). Green lines: LAGBs, white circles: deformation bands (DBs) in black lines, sb refer to the emerged subgrain boundaries in less deformed zones, I refers to initiation site of a crack at the intersection of slip band and grain boundary, II refers to initiation site of a crack at the intersection of slip band and subgrain boundary. (b) The corresponding kernel average misorientation (KAM) map showing the strain localisation. (For interpretation of the references to colour in this figure legend, the reader is referred to the Web version of this article.)

shown in Fig. 8(a).

The tensile flow curves at high temperatures, as depicted in Fig. 6, exhibit a notable softening effect, characterised by a drop in flow stress within the studied temperature range of 550–650 °C. This phenomenon is well-established and primarily attributed to the dynamic softening mechanisms (e.g., DRV and/or DRX) within the α-bcc ferritic structure during high-temperature deformation. Fig. 9(a) presents a BSE micrograph of the grain structure and the presence of the Laves phase after tensile testing at 550 °C. A prevalent feature of this image is the presence of serrated boundaries, primarily resulting from the ongoing plastic

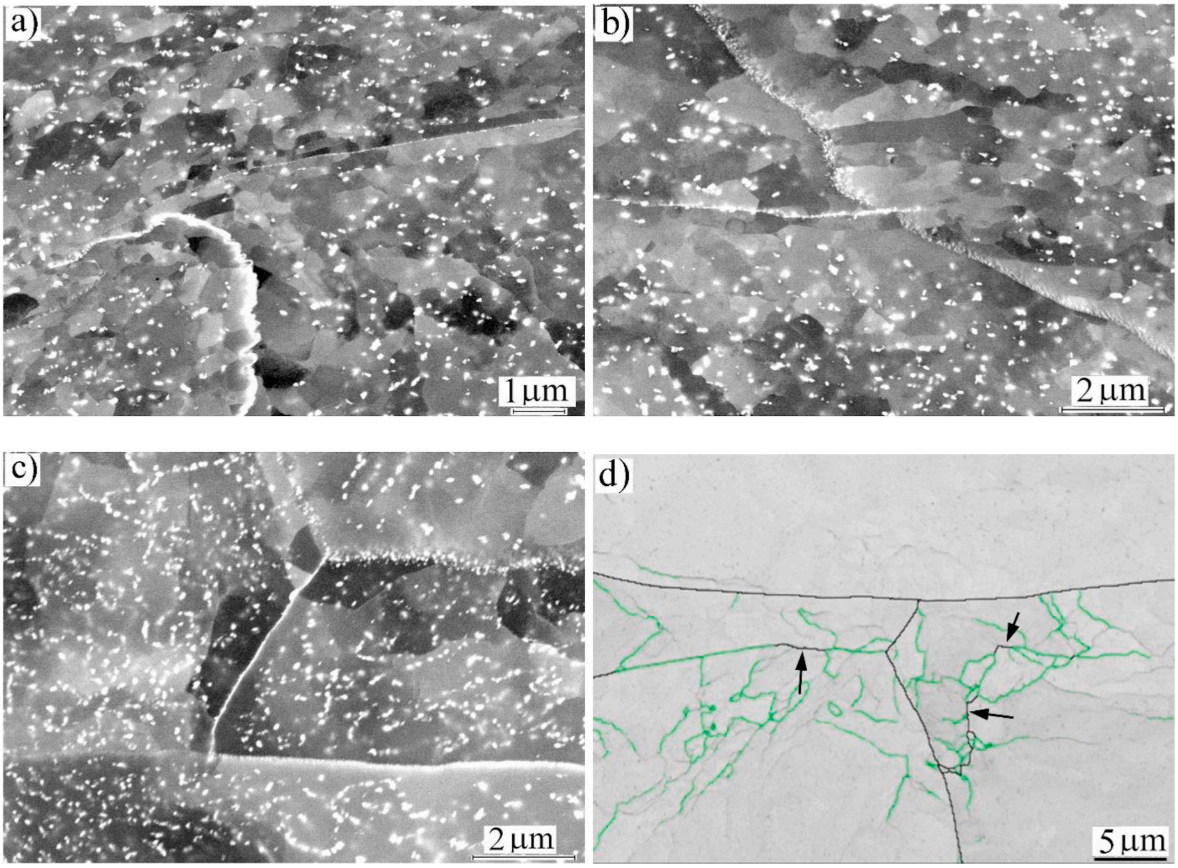

Fig. 9. Subgrain structure evolution of HiperFer^{SCR} at elevated temperatures: (a), (b) and (c) BSE micrographs of the deformed zones after tensile testing at 550 °C, 600 °C, and 650 °C, respectively. (d) EBSD-misorientation map showing LAGBs in green after tensile testing at 650 °C.

deformation along with the formation of subgrains within the interiors of the grains.

Similarly, the microstructural characteristics of the grain structure subjected to deformation at 600 °C are revealed in Fig. 9(b). In this case, sub-grains accompanied by Laves precipitates were observed. However, a notable distinction is the presence of relatively large elongated subgrains within the Laves PFZ surrounding the grain boundaries.

At 650 °C, as illustrated in Fig. 9(c)–a distinct subgrain structure emerges within the grain interiors. The misorientation map in Fig. 9(d)–as obtained by EBSD, primarily highlights the LAGBs (depicted in green, with misorientations of less than 15°), as well as the emergence of new HAGBs (denoted in black, with misorientations exceeding 15°) stemming from these subgrains within the deformed ferritic grains. This transformation indicated that certain LAGBs converted to HAGBs, marking the initiation of the DRX process. As established, the DRX mechanism is controlled by the rate of atomic diffusion, migration of grain or subgrain boundaries, and dislocation activity [47,48]. Despite the elevated temperature of 650 °C, DRX process within the studied HiperFer^{SCR} material remains notably sluggish. This is primarily attributed to the presence of nanosized Laves precipitates, which effectively hinder the activity of the subgrain boundaries and the DRX softening mechanism.

3.3.2. Microstructural characteristics at room temperature

Fig. 10 shows the microstructural characteristics of the samples subjected to tensile strain at room temperature. The IQ map coupled with misorientation map is shown in Fig. 9(a). Notably, fine traces of slip markings were discernible throughout the grain structure, for example, in grains G1, G2, and G3. These slip markings appear as non-indexed parallel lines, providing evidence of highly strained regions within the microstructure. A striking feature is the appearance of significant deformation bands with HAGBs (black lines) in the grains, highlighted by white circles. Furthermore, a substantial fraction of the LAGBs associated with the regions of the deformation bands were enhanced. The presence of LAGBs results from the accumulation of dislocations within the grain interiors during the straining process, and this phenomenon is significantly influenced by the extent of deformation and degree of recovery [49–51]. All these microstructural characteristics collectively contribute to the observed strain hardening driven by the slip deformation mechanism during plastic deformation, a phenomenon evident in the room-temperature tensile flow curve, as can be inferred from the tensile stress-strain curve depicted in Fig. 6.

The corresponding orientation map in Fig. 10(b) offers further insight into the microstructure achieved through tensile deformation at room temperature. The deformed microstructure exhibited a highly textured orientation. One series of adjacent grains showed a predominantly <001> orientation (red), and another series of adjacent grains displayed a <101> orientation (green). This was attributed to the high deformation of the material. Therefore, the substructure with a high fraction of LAGBs is enhanced in the interior of the grains. Consequently, the crystallographic orientations of adjacent grains were identical and relative to the deformation axis [52].

Within this microstructure, we observed two substantial cracks within the grain interiors, as indicated by the white ovals in Fig. 10 (b). The promotion of slip bands within the grains appears to correlate with the emergence of interior grain cracks. Additionally, cracks were visible along the boundaries, as indicated by the white arrows. To gain a clearer understanding of the relationship between slip bands and heightened crack features, BSE imaging was employed to visualise the microstructure. A notable finding in the BSE image in Fig. 10(c) is the presence of

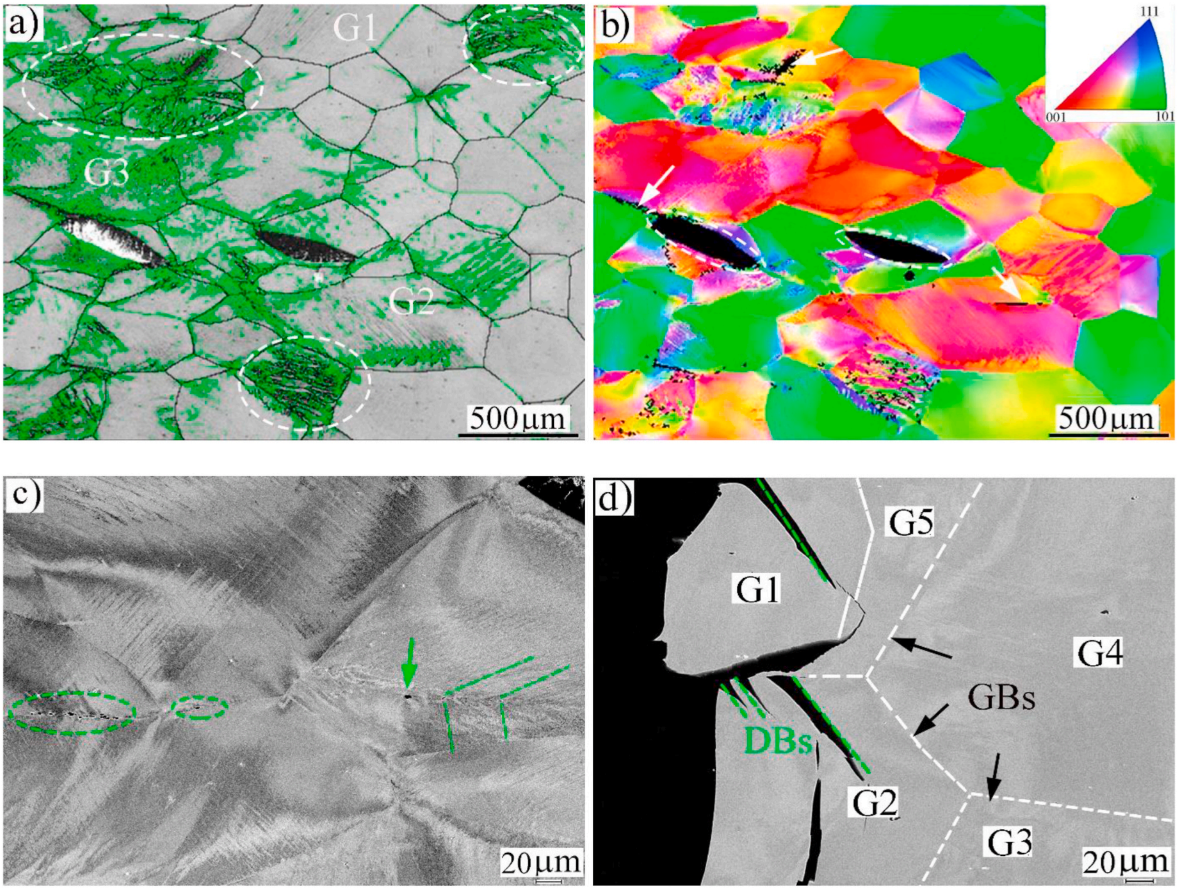

Fig. 10. Microstructural characteristics of HiperFer^{SCR} after tensile deformation at room temperature: (a) EBSD-misorientation map, LAGBs in green. (b) EBSD-orientation map, (c) high-magnification SEM-BSE image of the deformed zone indicating the crack initiation, and (d) longitudinal section of the fracture zone revealing the crack propagation along the deformation bands (DB)s in grain interiors. White dashed lines represent the grain boundaries (GBs) and Gx stands for grain number.

crack embryos at the intersection sites between the grain boundaries and slip bands, as highlighted by the green ovals. Furthermore, a crack embryo was observed within the interior of a grain, as indicated by the green arrow, at the intersection of the two slip bands. In contrast, in the fracture zone, which comprises five grains (G1–G5), as depicted in Fig. 10(d), the cracks are primarily confined to the grain interiors and are notably promoted along the deformation bands, which are clearly visible in G1 and G2. These deformation bands are highlighted by green dashed lines, signifying their crucial role in the propagation of cracks within the microstructure.

3.4. *Fracture characteristics and damage mechanism*

Fig. 11 provides a low-magnification overview of the fracture surface of the HiperFer^{SCR} steel following tensile testing at various temperatures, namely, room temperature, 550 °C, and 650 °C. In general, the fracture surfaces exhibit distinct characteristics depending on the test temperature. The fracture surface analysis at room temperature, as shown in Fig. 11(a), revealed several noteworthy features. The extensive fracture area encircled in yellow suggests that the material experienced a relatively low reduction in area during the tensile test (approximately 25 %) according to the flow curve in Fig. 6. This means that the material did not elongate significantly before fracturing compared to the attainable elongation at high temperatures. Additionally, the cleavage fracture pattern predominated, and surprisingly, there was an absence of a dimple zone, which is typical for ductile fractures. This unique fracture surface at room temperature signified a different damage mechanism from that activated for the samples tested at higher temperatures.

At higher temperatures of 550 °C and 650 °C, where Fig. 11(b) and (c) come into focus, the fracture surfaces present a similar appearance with relatively small fracture areas, which can be attributed to the higher reduction in area of 60 % and 73 %, respectively, for these temperature conditions. This observation strongly implies that RA, a measure of the ductility of the material, increases as the temperature increases. Furthermore, these fracture surfaces revealed the presence of regions featuring substantial voids in the size range of the entire grain, clearly marked by yellow circles, alongside zones with ductile fracture dimples. These large voids on the fracture surface subjected to high-temperature tensile straining are indicative of grain-boundary decohesion [53]. This type of cracking usually originates in the early stages of deformation and is often associated with grain-boundary sliding. As the hot deformation progressed, these cracks underwent distortion and ultimately evolved into elongated voids until the material reached its breaking point, as clearly depicted in Fig. 11(b) and (c). It is a reasonable inference that the dimples observed on the fracture surfaces are a consequence of ductile fracture mode of the material during the straining process at 550 °C and 650 °C.

The analysis of the deformation and damage mechanisms under tensile straining at different temperatures is further elucidated by closely examining the high-magnification images. Fig. 12, we explore the damage mechanism at room temperature. Fig. 12(a) shows the intergranular cracking along the grain boundaries, as indicated by the yellow dashed lines. Additionally, a high density of deformation slip markings, that is, slip bands formed as a consequence of the plastic

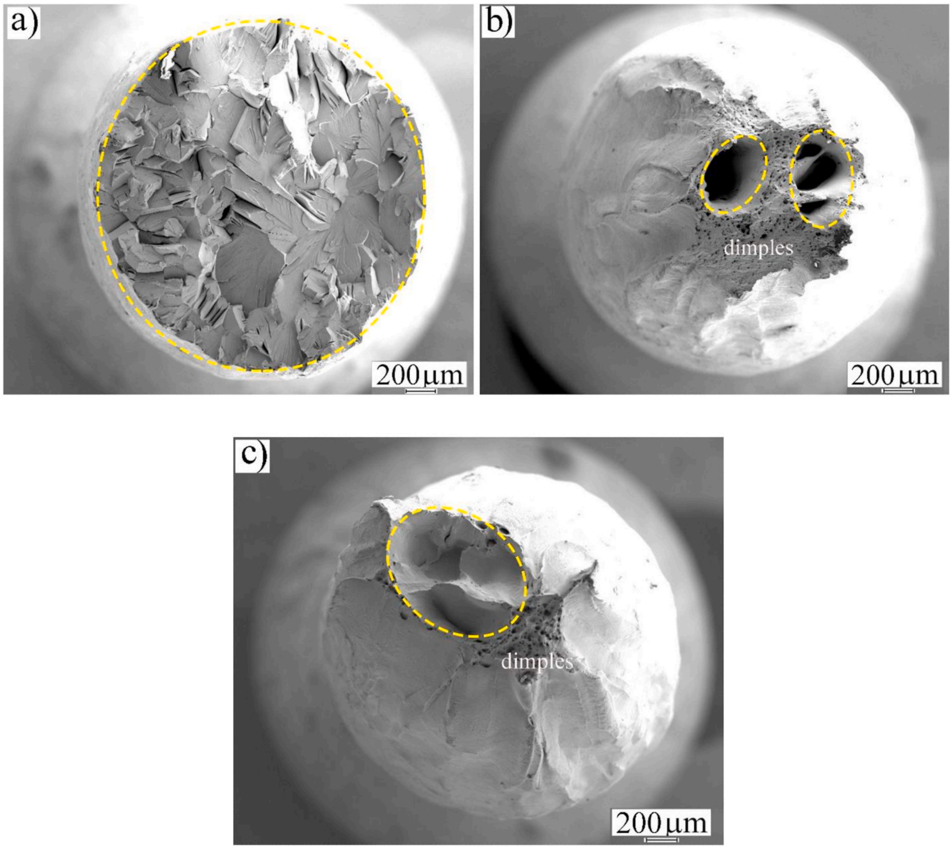

Fig. 11. SEM micrographs showing an overview of the fracture surfaces of HiperFer^{SCR} following Tensile testing at different temperatures: (a) room temperature, (b) 550 °C, and (c) 650 °C.

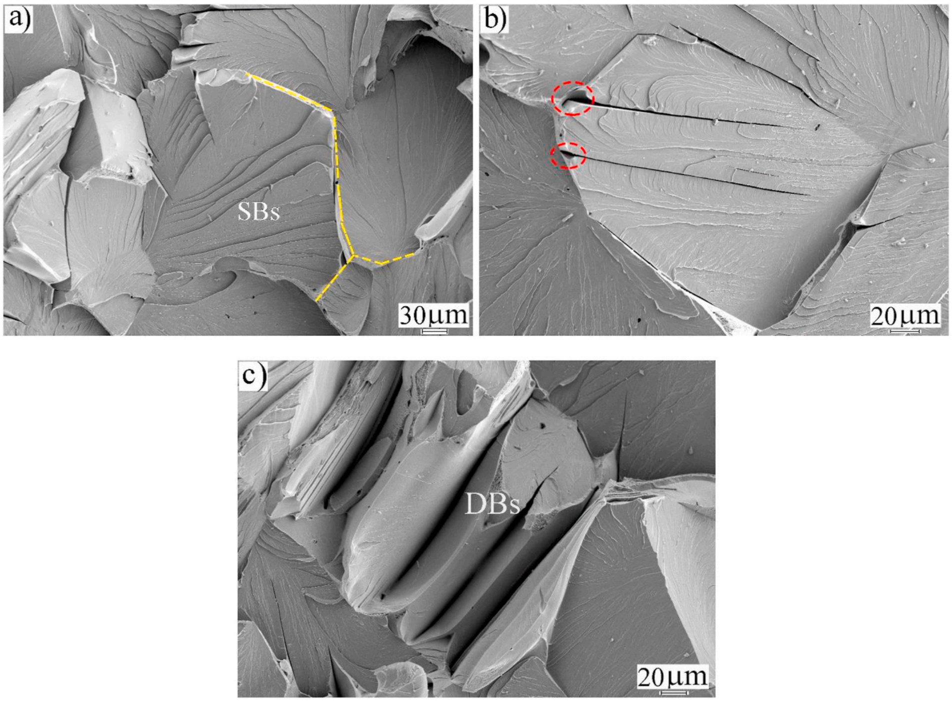

Fig. 12. SEM images of the fracture surface at room temperature revealing damage behaviour: (a) intergranular cracking alongside slip bands (SBs), (b) initiation of cracks at the intersections between slip bands and grain boundary, and their intergranular propagation as well as along slip bands in grain interior, and (c) cracks along deformation bands (DBs).

deformation of the structure, was also observed. As shown in Fig. 12(b), the flat grain surfaces in the presence of intergranular cracking are more apparent. Furthermore, we can clearly observe the initiation of cracks at the grain boundaries, primarily occurring at the intersection sites indicated by red circles, where slip bands intersect with grain boundaries. This phenomenon is consistent with the observations in the BSE image shown in Fig. 12(c). These intersections served as nucleation points for crack embryos along the grain boundaries, which subsequently propagated primarily through the grain boundaries, leading to intergranular cracking, as depicted in Fig. 12(a). In certain grains, these cracks extended through the deformation bands, which represent regions of highly localised strain, as shown in Fig. 12(b) and (c).

The correlation between the strain-hardening capacity and the fracture mechanisms under tensile straining was evident through a comparative analysis of the fracture surface characteristics of the steel at different temperatures. It is well-established that necking is initiated when the flow stress equals the strain-hardening rate during the tensile test. In instances where the steel exhibits a high strain-hardening rate induced by Laves phase particles, as observed for the HiperFer^{SCR} steel tested at room temperature, necking is facilitated during the latter stages of plastic deformation [54]. Consequently, the flow stress in the specimen can reach a level that induces shear instability in highly localised regions such as slip bands and grain boundaries. Subsequently, shear cracking manifested throughout the grain structure, specifically in the form of slip band cracking and grain boundary cracking, as shown in Fig. 12(a–c).

The examination of the fracture surface at 650 °C reveals key insights into the plastic deformation and damage behaviours within the material, particularly in the region highlighted by the yellow circle in Fig. 11(c). Upon closer inspection of this specific area, as shown in Fig. 13(a), we can clearly identify large voids where the grains (G1, G2, and G3) have decohered or separated from the matrix. Although the observed damage behaviour is controlled by a ductile mode, it seems that the fracture at high temperatures is induced by strain localisation at the grain boundaries, leading to intergranular decohesion, as is evident from the grain separation. Additionally, the strain localisation and formation of voids at the grain boundaries were prominently visible, as marked by red arrows in Fig. 13(a). Upon further magnification, Fig. 13(b) provides a more detailed view, showing parallel slip bands within the grain interiors but without signs of crack formation at the slip bands, in contrast to the damage behaviour at room temperature. Concurrently, small pores at the grain boundaries were promoted, suggesting the presence of localised strain and damage in these areas. This pattern became even more apparent when we closely examined the highlighted zone in Fig. 13(b)–as shown in Fig. 13(c). A few pores were observed at the grain boundaries along with deformation bands. It appears that the microcracks extend through the grain boundaries, as indicated by the red arrows. Notably, a particular grain boundary segment is highlighted by the red dashed-line rectangular box in Fig. 13(a), where the local deformation along the grain boundary is evident. From these observations, it becomes clear that the damage behaviour of HiperFer^{SCR} at high temperatures (in this case at 650 °C) primarily initiates at grain boundaries not a mixed-type as observed for the specimen tested at room temperature showing damage initiation at grain boundaries as well as inside grains. The measurements of the width of the PFZ after the tensile tests indicated an increase in the average width of the specimens deformed at high temperatures compared with that measured after testing at room temperature, as shown in Fig. 14. This widening of the PFZ is associated with the growth of larger particles at the expense of smaller ones during high-temperature deformation. The high-temperature-induced widening of the PFZ (in other words, the absence of Laves phase precipitates in the vicinity of the grain boundaries) allows strain localisation that contributes to intergranular decohesion. At high temperatures, the weakness of the grain boundaries is exacerbated, leading to the initiation of intergranular cracking.

This study provides several insights into the high-temperature deformation and damage behaviours of the newly developed HiperFer^{SCR} proposed for CSP applications, where high corrosion resistance against molten salt, microstructural stability, and excellent mechanical properties at high temperatures are mandatory. The solar-salt corrosion

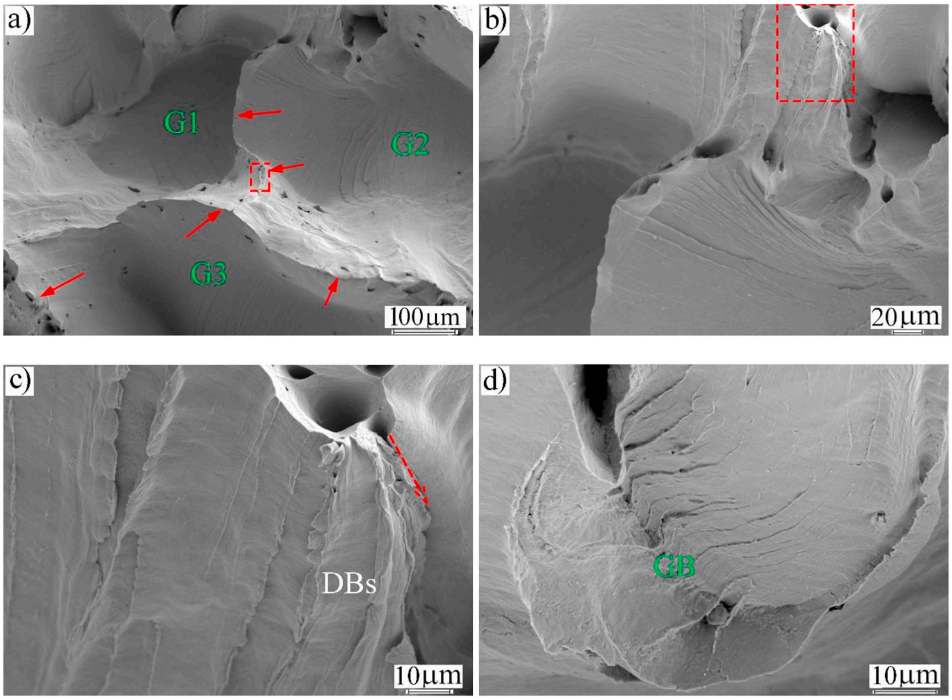

Fig. 13. SEM images of the fracture surface at 650 °C revealing the main characteristics of damage evolution: (a) strain localisation at grain boundaries (Gbs) accompanied by void formations leading to grain boundary decohesion and eventually grain separation. G1, G2 and G3 refer to the places of respective grains. (b) Formation of voids at grain boundary, (c) magnified view of the highlighted region in (b) showing deformation bands (DBs), and (d) crack along a grain boundary.

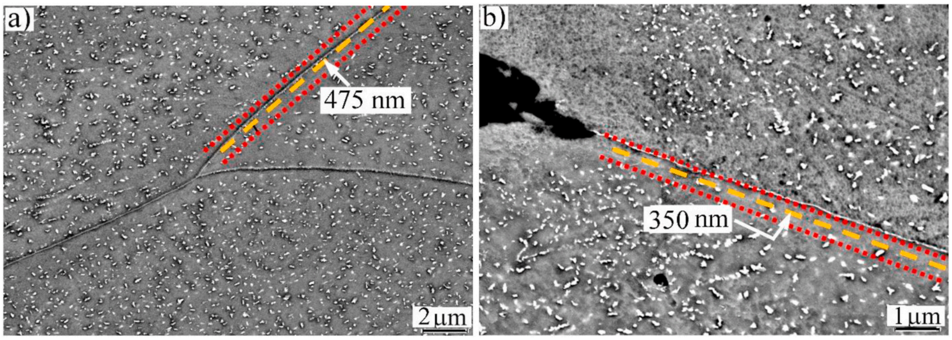

Fig. 14. SEM images near fracture zones of tensile-tested specimen showing the average width of PFZ after testing at different temperatures: a) at 650 °C and b) at room temperature.

resistance of model alloys (as a development step of HiperFer^{SCR}) has been reported, emphasising the promising opportunity to replace expensive austenitic alloys with HiperFer^{SCR} for CSP [23]. However, this study focused on deformation and damage behaviours at high temperatures, and future reports on fatigue and creep life will follow. It is clear that Laves phase particles are responsible for strain hardening at room temperature and control the extent of strain softening at high temperatures by allowing DRV while restricting DRX. Furthermore, the damage appeared to be stimulated by the intersections of deformation-induced slip bands and grain boundaries at room temperature, resulting in cracking along both the grain boundaries and in the grain interior along the slip bands. At high temperatures, damage is caused by strain localisation in the PFZ, leading to grain boundary decohesion, while the ductile fracture mode is still dominant. These findings suggest the need to further adjustments of the process parameters to optimise the Laves phase precipitation and the width of PFZ, in order to qualify the HiperFer^{SCR} to CSP applications in the temperature range 550–650 °C.

4. Conclusions

A newly developed high-performance ferrite and salt-corrosion resistant (HiperFer^{SCR}) steel was manufactured and thermomechanically processed to prepare a ferritic microstructure containing Laves phase particles of type (Fe,Cr, Si)$_2$(Nb,W). Tensile tests at high temperatures (550, 600, 650 °C) as well as at room temperature alongside comprehensive microstructural and fracture surfaces analyses were carried out to explore the respective deformation and damage behaviours. The investigation yielded significant insights, and the key findings and implications are as follows.

1 The HiperFer^{SCR} steel displays distinctive mechanical characteristics at room temperature, manifesting a noteworthy strain-hardening effect that results in high yield and tensile strengths of approximately 500 and 720 MPa, respectively. Such high strength levels and strain-hardening capacities at room temperature are attributed to the ferritic matrix strengthened with Laves phase particles, which facilitate the generation of a high density of slip bands during deformation.

2 With an increase in the tensile-test temperature to the range of 550–650 °C, a significant strain softening is promoted during the plastic deformation, which is ascribed to the activation of DRV mechanism. Microstructural analysis subsequent to the high-temperature tensile tests revealed the emergence of subgrain boundaries decorated with Laves phase particles that suppressed DRX.

3 A pronounced divergence in the damage behaviour of the HiperFer^{SCR} steel was observed between the room- and high-temperature deformations. At room temperature, the tensile strain was accommodated by the generation of slip bands, and damage initiation occurred at the intersections between the slip bands and grain boundaries. Both intergranular cracking and slip band cracking were prominent during the room-temperature deformation.

4 During high-temperature deformation, the tensile strain is dissipated through DRV and the formation of slip bands within the grain interior. Nevertheless, strain localisation and void formation are enhanced at the grain boundaries owing to the considerable widening of the PFZ, which leads to intergranular decohesion while maintaining a ductile fracture mode.

5 The current study demonstrated the significant role of Laves phase particles in determining the deformation and damage modes in HiperFer^{SCR} steel and emphasised the need for further adjustments of their precipitation behaviour (e.g. reducing PFZ) to limit grain boundary decohesion at high temperatures despite the observed ductile fracture.

CRediT authorship contribution statement

Atef Hamada: Writing – review & editing, Writing – original draft, Visualization, Investigation, Formal analysis. **Fadoua Aarab:** Writing – original draft, Methodology, Formal analysis, Writing – review & editing. **Ruth Schwaiger:** Writing – review & editing, Supervision, Resources. **Tarek Allam:** Writing – review & editing, Writing – original draft, Supervision, Project administration, Conceptualization.

Declaration of competing interest

The authors declare that they have no known competing financial interests or personal relationships that could have appeared to influence the work reported in this paper.

Data availability

Data will be made available on request.

Acknowledgment

The authors acknowledge the German Federal Ministry of Education and Research (BMBF) for the support under grant number 03EE5048D. Dr. Egbert Wessel and Dr. Daniel Grüner, Institute of Energy and Climate Research – Structure and Function of materials (IEK-2) are acknowledged for operating the microscope.

References

[1] B.K. Kim, Y.S. Ko, I.H. Jung, H.N. Han, K.W. Yi, D.I. Kim, Role of the alloy grain boundaries in the high-temperature oxidation and Cr volatilization of 22 wt% Cr ferritic stainless steel for SOFC applications, Corrosion Sci. 213 (2023) 110940, https://doi.org/10.1016/J.CORSCI.2022.110940.

[2] Y. Zhao, H.L. Liu, L.L. Wei, L.Q. Chen, An overview on the novel heat-resistant ferritic stainless steels, Tungsten 5 (2023) 467–480, https://doi.org/10.1007/s42864-022-00171-4.

[3] M. Jiang, Y. Han, J. Sun, G. Zu, W. Zhu, X. Song, Y. Song, X. Ran, Enhancing oxidation resistance of ferritic heat-resistant stainless steel in air atmosphere at 1100 °C by self-repairing oxide layer, Mater. Char. 208 (2024) 113619, https://doi.org/10.1016/J.MATCHAR.2023.113619.

[4] X. Cheng, Z. Jiang, D. Wei, J. Zhao, B.J. Monaghan, R.J. Longbottom, L. Jiang, High temperature oxidation behaviour of ferritic stainless steel SUS 430 in humid air, Met. Mater. Int. 21 (2015) 251–259, https://doi.org/10.1007/S12540-015-4168-5/METRICS.

[5] X. Fan, B. Kuhn, J. Pöpperlová, W. Bleck, U. Krupp, Compositional optimization of high-performance ferritic (HiperFer) steels—effect of niobium and tungsten content, Met 10 (2020) 1300, https://doi.org/10.3390/MET10101300, 10 (2020) 1300.

[6] B. Kuhn, M. Talik, Impact of processing on the creep properties of high performance ferritic (HiperFer) steels, Met. 12 (2022) 1459, https://doi.org/10.3390/MET12091459, 12 (2022) 1459.

[7] J. Lopez Barrilao, B. Kuhn, E. Wessel, Microstructure evolution and dislocation behaviour in high chromium, fully ferritic steels strengthened by intermetallic Laves phases, Micron 108 (2018) 11–18, https://doi.org/10.1016/J.MICRON.2018.02.008.

[8] F.X. Fan, Optimization of Laves Phase Strengthened High Performance Ferritic Stainless Steels, 2020.

[9] J. Froitzheim, G.H. Meier, L. Niewolak, P.J. Ennis, H. Hattendorf, L. Singheiser, W. J. Quadakkers, Development of high strength ferritic steel for interconnect application in SOFCs, J. Power Sources 178 (2008) 163–173, https://doi.org/10.1016/J.JPOWSOUR.2007.12.028.

[10] B. Kuhn, C.A. Jimenez, L. Niewolak, T. Hüttel, T. Beck, H. Hattendorf, L. Singheiser, W.J. Quadakkers, Effect of Laves phase strengthening on the mechanical properties of high Cr ferritic steels for solid oxide fuel cell interconnect application, Mater. Sci. Eng. 528 (2011) 5888–5899, https://doi.org/10.1016/J.MSEA.2011.03.112.

[11] B. Kuhn, M. Talik, T. Fischer, X. Fan, Y. Yamamoto, J.L. Barrilao, Science and technology of high performance ferritic (HiperFer) stainless steels, Met. 10 (2020) 463, https://doi.org/10.3390/MET10040463, 10 (2020) 463.

[12] S. Möller, B. Kuhn, R. Rayaprolu, S. Heuer, M. Rasinski, A. Kreter, HiperFer, a reduced activation ferritic steel tested for nuclear fusion applications, Nucl. Mater. Energy. 17 (2018) 9–14, https://doi.org/10.1016/j.nme.2018.06.010.

[13] F. Stein, A. Leineweber, Laves phases: a review of their functional and structural applications and an improved fundamental understanding of stability and properties, J. Mater. Sci. 56 (2021) 5321–5427, https://doi.org/10.1007/s10853-020-05509-2.

[14] S. Kobayashi, K. Kimura, K. Tsuzaki, Interphase precipitation of Fe2Hf Laves phase in a Fe–9Cr/Fe–9Cr–Hf diffusion couple, Intermetallics 46 (2014) 80–84, https://doi.org/10.1016/J.INTERMET.2013.10.017.

[15] S. Kobayashi, T. Hibaru, Formation of the Fe2Hf Laves phase along the eutectoid-type reaction path of δ-Fe→γ-Fe+Fe2Hf in an Fe-9Cr based alloy, ISIJ Int. 55 (2015) 293–299, https://doi.org/10.2355/ISIJINTERNATIONAL.55.293.

[16] J. Hald, Microstructure and long-term creep properties of 9–12% Cr steels, Int. J. Pres. Ves. Pip. 85 (2008) 30–37, https://doi.org/10.1016/J.IJPVP.2007.06.010.

[17] N. Nabiran, S. Klein, S. Weber, W. Theisen, Evolution of the Laves phase in ferritic heat-resistant steels during long-term annealing and its influence on the high-temperature strength, Metall. Mater. Trans. A 46 (2015) 102–114, https://doi.org/10.1007/S11661-014-2505-9/TABLES/7.

[18] H.H. Lu, H.K. Guo, W. Liang, J.C. Li, G.W. Zhang, T.T. Li, High-temperature Laves precipitation and its effects on recrystallisation behaviour and Lüders deformation in super ferritic stainless steels, Mater. Des. 188 (2020) 108477, https://doi.org/10.1016/J.MATDES.2020.108477.

[19] Z. Sun, P.D. Edmondson, Y. Yamamoto, Effects of Laves phase particles on recovery and recrystallization behaviors of Nb-containing FeCrAl alloys, Acta Mater. 144 (2018) 716–727, https://doi.org/10.1016/J.ACTAMAT.2017.11.027.

[20] M. Żuk, A. Czupryński, D. Czarnecki, T. Poloczek, The effect of niobium and titanium in base metal and filler metal on intergranular corrosion of stainless steels, Weld. Technol. Rev. 91 (2019) 30–38, https://doi.org/10.26628/WTR.V91I6.1032.

[21] J.L. Barrilao, B. Kuhn, E. Wessel, Microstructure and intermetallic particle evolution in fully ferritic steels, Adv. Mater. Technol. Foss. Power Plant (2016) 1027–1035.

[22] J. Klöwer, Factors affecting the oxidation behaviour of thin Fe-Cr-AI foils Part II: the effect of alloying elements: overdoping, Werkstoffe Korrosion 51 (2000) 373–385, https://doi.org/10.1002/(sici)1521-4176(200005)51:5<373::aid-maco373>3.0.co;2-o.

[23] F. Aarab, B. Kuhn, Development of self-passivating, high-strength ferritic alloys for concentrating solar power (CSP) and thermal energy storage (TES) applications, Energies 16 (2023) 4084, https://doi.org/10.3390/EN16104084, 16 (2023) 4084.

[24] F. Aarab, B. Kuhn, A. Bonk, T. Bauer, A new approach to low-cost, solar salt-resistant structural materials for concentrating solar power (CSP) and thermal, Energy Storage Mater. 11 (2021) 1970, https://doi.org/10.3390/MET11121970, 11 (2021) 1970.

[25] M. Palm, Phase equilibria in the Fe corner of the Fe–Al–Nb system between 800 and 1150 °C, J. Alloys Compd. 475 (2009) 173–177, https://doi.org/10.1016/J.JALLCOM.2008.07.036.

[26] A.S. Hamada, L.P. Karjalainen, M.C. Somani, R.M. Ramadan, Deformation mechanisms in high-al bearing high-Mn TWIP Steels in hot compression and in tension at low temperatures, Mater. Sci. Forum 550 (2007) 217–222, https://doi.org/10.4028/0-87849-434-0.217.

[27] A. Hamada, T. Juuti, A. Khosravifard, A. Kisko, P. Karjalainen, D. Porter, J. Kömi, Effect of silicon on the hot deformation behavior of microalloyed TWIP-type stainless steels, Mater. Des. 154 (2018) 117–129, https://doi.org/10.1016/J.MATDES.2018.05.029.

[28] B. Kuhn, M. Talik, HiperFer – high performance ferritic steels – HIGH PERFORMANCE FERRITIC STEELS, in: Proc. 10th Liége Conf. Mater. Adv. Power Eng., 2015, pp. 264–273. Liége, Belgium.

[29] D.J. Abson, J.S. Rothwell, Review of type IV cracking of weldments in 9–12%Cr creep strength enhanced ferritic steels, Int. Mater. Rev. 58 (2013) 437–473, https://doi.org/10.1179/1743280412Y.0000000016.

[30] M. Igarashi, Alloy design philosophy of creep-resistant steels, in: R. Abe, F. Kern, T. U. Viswanathan (Eds.), Creep-Resistant Steels, Woodhead Publishing, Cambridge, UK, 2008, pp. 539–572, https://doi.org/10.1533/9781845694012.3.539.

[31] T. Maitland, S. Sitzman, Backscattering detector and EBSD in nanomaterials characterization, in: Z.L. Zhou, W. Wang (Eds.), Scanning Microsc. Nanotechnol. Tech. Appl., Springer, New York, New York, NY, 2007, pp. 41–75, https://doi.org/10.1007/978-0-387-39620-0_2.

[32] B. Kuhn, M. Talik, Heat treatment of high-performance ferritic (HiperFer) steels, Materials 16 (2023) 3500, https://doi.org/10.3390/MA16093500, 16 (2023) 3500.

[33] J. Pöpperlová, D. Wipp, B. Kuhn, W. Bleck, Laves phase precipitation behavior in HiperFer (high performance ferritic) steel with and without boron alloying, Met 13 (2023) 235, https://doi.org/10.3390/MET13020235, 13 (2023) 235.

[34] G.M. Sim, J.C. Ahn, S.C. Hong, K.J. Lee, K.S. Lee, Effect of Nb precipitate coarsening on the high temperature strength in Nb containing ferritic stainless steels, Mater. Sci. Eng. 396 (2005) 159–165, https://doi.org/10.1016/J.MSEA.2005.01.030.

[35] N. Fujita, K. Ohmura, A. Yamamoto, Changes of microstructures and high temperature properties during high temperature service of Niobium added ferritic stainless steels, Mater. Sci. Eng. 351 (2003) 272–281, https://doi.org/10.1016/S0921-5093(02)00831-6.

[36] N. Oono, H. Nitta, Y. Iijima, Diffusion of niobium in α-iron, Mater. Trans. 44 (2003) 2078–2083, https://doi.org/10.2320/MATERTRANS.44.2078.

[37] B. Kuhn, M. Talik, L. Niewolak, J. Zurek, H. Hattendorf, P.J. Ennis, W. J. Quadakkers, T. Beck, L. Singheiser, Development of high chromium ferritic steels strengthened by intermetallic phases, Mater. Sci. Eng. 594 (2014) 372–380, https://doi.org/10.1016/J.MSEA.2013.11.048.

[38] L. Niewolak, A. Savenko, D. Grüner, H. Hattendorf, U. Breuer, W.J. Quadakkers, Temperature dependence of Laves phase composition in Nb, W and Si-alloyed high chromium ferritic steels for SOFC interconnect applications, J. Phase Equilibria Diffus. 36 (2015) 471–484, https://doi.org/10.1007/S11669-015-0403-5/TABLES/4.

[39] Y. Kato, M. Ito, Y. Kato, O. Furukimi, Effect of Si on precipitation behavior of Nb-Laves phase and amount of Nb in solid solution at elevated temperature in high purity 17%Cr-0.5%Nb steels, Mater. Trans. 51 (2010) 1531–1535, https://doi.org/10.2320/MATERTRANS.M2010112.

[40] S.V. Mehtonen, E.J. Palmiere, R.D.K. Misra, L.P. Karjalainen, D.A. Porter, Dynamic restoration mechanisms in a Ti–Nb stabilized ferritic stainless steel during hot deformation, Mater. Sci. Eng. 601 (2014) 7–19, https://doi.org/10.1016/J.MSEA.2014.02.039.

[41] H. Khatami-Hamedani, A. Zarei-Hanzaki, H.R. Abedi, A.S. Anoushe, L. P. Karjalainen, Dynamic restoration of the ferrite and austenite phases during hot compressive deformation of a lean duplex stainless steel, Mater. Sci. Eng. 788 (2020) 139400, https://doi.org/10.1016/J.MSEA.2020.139400.

[42] C. Castan, F. Montheillet, A. Perlade, Dynamic recrystallization mechanisms of an Fe–8% Al low density steel under hot rolling conditions, Scripta Mater. 68 (2013) 360–364, https://doi.org/10.1016/J.SCRIPTAMAT.2012.07.037.

[43] H.R. Abedi, A. Zarei Hanzaki, Z. Liu, R. Xin, N. Haghdadi, P.D. Hodgson, Continuous dynamic recrystallization in low density steel, Mater. Des. 114 (2017) 55–64, https://doi.org/10.1016/J.MATDES.2016.10.044.

[44] P. Cizek, The microstructure evolution and softening processes during high-temperature deformation of a 21Cr–10Ni–3Mo duplex stainless steel, Acta Mater. 106 (2016) 129–143, https://doi.org/10.1016/J.ACTAMAT.2016.01.012.

[45] S. Ghosh, A. Hamada, M. Patnamsetty, W. Borek, M. Gouda, A. Chiba, S. Ebied, Constitutive modeling and hot deformation processing map of a new biomaterial Ti–14Cr alloy, J. Mater. Res. Technol. 20 (2022) 4097–4113, https://doi.org/10.1016/J.JMRT.2022.08.160.

[46] T. Zhao, Y. Hu, B. He, C. Zhang, T. Zheng, F. Pan, Effect of manganese on microstructure and properties of Mg-2Gd magnesium alloy, Mater. Sci. Eng. 765 (2019) 138292, https://doi.org/10.1016/J.MSEA.2019.138292.

[47] F.J. Humphreys, M. Hatherly, Recrystallization and Related Annealing Phenomena, second ed., Elsevier Science, New York, 2012 https://doi.org/10.1016/C2009-0-07986-0.

[48] M. Ali, A. Khosravifard, A. Hamada, T. Mattar, M. Eissa, J. Kömi, Promotion of thermomechanical processing of 2-GPa low-alloyed ultrahigh-strength steel and physically based modelling of the deformation behaviour, Mater. Sci. Eng. 867 (2023) 144747, https://doi.org/10.1016/J.MSEA.2023.144747.

[49] X. Xu, M. Hao, J. Chen, W. He, G. Li, C. Jiao, T.L. Burnett, X. Zhou, Influence of microstructural and crystallographic inhomogeneity on tensile anisotropy in thick-section Al–Li–Cu–Mg plates, Mater. Sci. Eng. 829 (2022) 142135, https://doi.org/10.1016/J.MSEA.2021.142135.

[50] H.J. McQueen, E. Evangelista, Substructures in aluminium from dynamic and static recovery, Czechoslov, J. Phys. 38 (1988) 359–372, https://doi.org/10.1007/BF01605405/METRICS.

[51] M.T. Pérez-Prado, J.A. Del Valle, J.M. Contreras, O.A. Ruano, Microstructural evolution during large strain hot rolling of an AM60 Mg alloy, Scripta Mater. 50 (2004) 661–665, https://doi.org/10.1016/J.SCRIPTAMAT.2003.11.014.

[52] G. Azimi-Roeen, S.F. Kashani-Bozorg, M. Nosko, L. Orovcik, EBSD investigation of Al/(Al13Fe4+Al2O3) nanocomposites fabricated by mechanical milling and friction stir processing, J. Microsc. 270 (2018) 3–16, https://doi.org/10.1111/JMI.12642.

[53] A.S. Hamada, L.P. Karjalainen, Hot ductility behaviour of high-Mn TWIP steels, Mater. Sci. Eng. 528 (2011) 1819–1827, https://doi.org/10.1016/J.MSEA.2010.11.030.

[54] Z.C. Luo, M.X. Huang, Revealing the fracture mechanism of twinning-induced plasticity steels, Steel Res. Int. 89 (2018) 1700433, https://doi.org/10.1002/SRIN.201700433.